

Preliminary Methods for Modeling Stress-Strain Curves of Human Ribs from Structural Dynamic Bending Tests

Molly Tillis, Scott Stuckey, Akshara Sreedhar, Jason Stammen, Kevin Moorhouse, Amanda Agnew, Yun-Seok Kang

Abstract It is important to understand and quantify rib behavior in dynamic impacts because thorax injuries are common in motor vehicle crashes and have a high incidence of morbidity and mortality. The goal of this research was to develop a preliminary method to calculate stress and stress-strain curves for which a quantitative model could be used to identify material properties from structural rib tests. Dynamic bending experiments were successfully conducted on 30 whole, mid-level, excised ribs affixed with uniaxial strain gages. A custom MATLAB code was created to calculate stress based on precise cross-sectional geometry at the fracture location. In combination with the strain data, stress-strain curves were created, and a continuous piecewise model was successfully developed to characterize each curve. This model was based on multiple parameters that were used to describe the linear elastic and plastic portion of the stress-strain curve. The model revealed an excellent fit for the stress-strain curves with R^2 values ranging from 0.985 - 0.999. Because of the high degree of fit, material properties were extracted directly from the model. Elastic modulus values were overestimated by the model and future work is needed to obtain more accurate results. This model seeks to provide a new method of extracting specific material parameters that could be applied to a large, existing experimental rib fracture data set.

Keywords material properties, rib fracture, stress-strain curves, structural test

I. INTRODUCTION

Thoracic injuries are particularly prevalent in motor vehicle crashes and have a high associated risk of morbidity and mortality. According to Liu *et al.* [1], severe injuries (AIS4-6)[2] occur disproportionately in the thorax and the incidence of thoracic injury increases with age. Additionally, it has been shown that more severe thorax AIS scores are predictive of patient mortality and this predictive accuracy increases with patient age [3]. Specifically, adults over 64 years hospitalized with severe rib fractures due to a motor vehicle crash (MVC) are 2.5 times more likely to die than those who were hospitalized with non-rib injuries. In contrast, younger patients were only 1.4 times more likely to die than their counterparts with non-rib injuries [3]. This increased mortality can be due to the injury itself or to secondary complications, such as respiratory failure, pneumonia, or pulmonary contusions [4]. This information indicates the need to further explore rib properties across the population in order to understand differential fracture risk.

The bulk of protection to the vital thoracic organs comes from the rib cage so understanding the behavior and properties of individual ribs is of interest as whole ribs are the units which comprise the rib cage. Material properties are important for constructing finite element (FE) rib models which are useful for evaluating the effectiveness of thorax injury mitigation strategies [5][6]. The accuracy of FE models is increased with the use of subject-specific material properties obtained from experimental testing [7] rather than relying solely on scaling and morphing techniques. Similarly, structural properties are important to consider and could be evaluated from subject-specific testing to accurately represent a particular human demographic. It is also important to capture the variation present in material and structural rib properties across human populations. Understanding this variation is an important step towards understanding how and why different populations are more vulnerable in certain crash scenarios.

Previous studies have examined the material of rib cortical bone [8-12] and the structural properties of ribs [13-24] independently. Some have even explored the structural and material properties of ribs through structural

M. Tillis (email:tillis.16@osu.edu) is a M.S. student in Biomedical Engineering at The Ohio State University in Columbus, OH, USA. M. Tillis, SP Stuckey, A Sreedhar, YS Kang and AM Agnew are affiliated with the Injury Biomechanics Research Center (IBRC) at The Ohio State University, Columbus, OH, USA. J. Stammen and K. Moorhouse are affiliated with the National Highway Traffic Safety Administration, Vehicle Research and Test Center (NHTSA/VRTC) in East Liberty, OH, USA.

tests of whole excised ribs and subsequent tensile material tests for coupons of rib cortical bone from the same subjects [5][6]. Despite existing data regarding the material and structural properties of ribs, there has been little work done to link properties across the anatomical hierarchy (i.e., tissue, organ, region, whole body, etc.), thereby contextualizing material properties within the structural behavior of ribs. Therefore, the objectives of this study, based on dynamic whole rib anterior-posterior (A-P) bending experiments, were to: 1) explore the feasibility of a method for calculating rib stress, and 2) generate stress-strain curves for which a quantitative model could be derived in order to predict material response from structural experimentation.

II. METHODS

Experimental Testing

Thirty whole ribs from 30 individuals (16 male, 14 female) aged 24 to 97 years (mean 63.8 ± 20.8) were used in this study. Samples were obtained ethically from the Body Donation Program at The Ohio State University and Lifeline of Ohio. Each rib, hydrated and prepared as in Agnew et al. [13], was tested to failure in a dynamic anterior-posterior impact with force, moment, displacement, and strain measured throughout the duration of the event by a six-axis load cell (CRABI neck load cell, IF-954, Humanetics, Plymouth, MI, USA), string potentiometer (Rayelco P-20A, AMETEK, Inc., Berwyn, PA, USA), and four uniaxial strain gages (Vishay Micro-Measurement, CEA-06-062UW-350, Shelton, CT), respectively (Figure 1). A 54 kg pendulum impacted the sternal end of the rib and translated it towards the vertebral end, thereby bending the entire specimen until failure. Due to the nature of the test, the cutaneous cortex was loaded in tension, while the pleural cortex was loaded in compression. Four strain gages were attached to the rib at 30% (location 1) and 60% (location 2) from the vertebral end of the curve length on the pleural and cutaneous cortices (Figure 2), and the load cell was fixed behind the vertebral end plate to measure the reaction forces and moments. The 2 m/s impact velocity applied here corresponded to an average strain rate of 0.5 strain/sec, which is representative of rib strain rate experienced during belt loading in a table-top belt loading test reconstructing a realistic crash scenario at 48 kph [25]. Full details of the rib test set-up and data processing can be found in Agnew et al. [13].

Each rib was marked at approximately every centimeter along the curve length, and high-speed video (Phantom, Vision Research, Inc., Fort Wayne, IN, USA) was obtained for each test at 1000 fps. The local displacement in the xy-plane of these marks were measured using TEMA video analysis software (Image Systems AB, Linköping, Sweden). A whole histological cross-section was obtained directly adjacent to each fracture, and high-resolution images (1446 pix/mm) were taken of each cross-section. ImageJ software (NIH) was used to calculate cortical area and cortical section radius for the cutaneous cortex from the high-resolution cross-section images as outlined in [26][27]. Each rib (n=30) had four strain gages, but because bone is known to fracture at lower stresses in tension than in compression [28] and material testing on cortical bone is typically performed in tension [8-12], only one gage on the cutaneous cortex of the rib closest to the fracture location was considered in this preliminary study. Only the fracture closest to the strain gages at location 2 was used for ribs that sustained more than one fracture. All measurements and calculations were relative to this cutaneous gage location. Thus, a total of 30 stress-strain curves were evaluated.

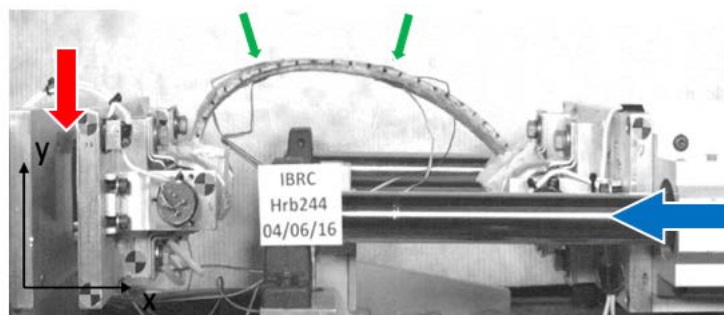


Fig. 1. Exemplar rib in the test fixture. Left arrow shows the location of the load cell, two small arrows in the center show strain gage locations on the cutaneous cortex, one of which was used for creating the stress-strain curve (whichever was nearest to fracture location). The large arrow to the right shows the impact direction. Small black marks along the length of the specimen were used to track the local displacement of the rib through the test in the xy-plane (TEMA points). The sternal end of the rib is on the right and the vertebral end of the rib is on the left.

Stress Calculation and Modeling

The load cell data were filtered using Channel Frequency Class (CFC) 180 [29], but strain data were left unfiltered as signal noise did not affect the fitting of the model. Additionally, the TEMA data were up-sampled from 1,000 Hz to 20,000 Hz via linear interpolation to match the sampling rate of the strain gages and load cell. A custom MATLAB code was created to calculate stress and plot the stress-strain curves based on the physical parameters and instrumentation shown in Figures 1 and 2.

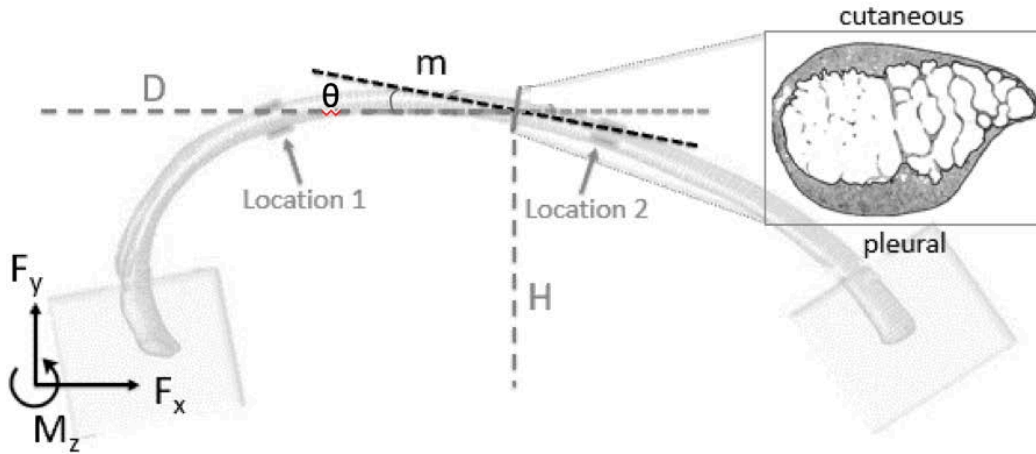


Fig. 2. Equation parameters on a rib. All parameters except F_x , F_y , and M_z are dependent on the location of the cross-section along the rib.

Based on curved beam theory [30], the equation for normal stress caused by the axial load, σ_n (MPa), at any given cross-section along the length of the rib was calculated:

$$\sigma_n = \frac{F_x \cos \theta + F_y \sin \theta}{Ct.Ar}, \tag{1}$$

where F_x and F_y are the x- and y-forces (N), respectively, θ is the angle of the cross-section relative to horizontal (degrees) and $Ct.Ar$ is the cortical area (mm^2) of the cross-section. The TEMA points were used to calculate θ by fitting the points on the rib to a 6th order polynomial and calculating the slope of the rib section at the point of the cross-section(s) throughout the duration of the test, by the equation:

$$\tan \theta = \frac{\Delta y}{\Delta x} = m \rightarrow \theta = \arctan(m), \tag{2}$$

where Δx and Δy are the local change in x- and y-space (mm), respectively, and m is the slope (unitless). The equation for normal stress caused by the bending moment is:

$$\sigma_b = \frac{MR(R-e-c)}{Ic}, \tag{3}$$

where M is the total bending moment (N-mm), R is the radius of curvature of the rib (mm), e is the distance from the centroidal axis to the neutral axis (mm), c is the maximum radius of the cross-section from the centroidal axis to the cutaneous surface (mm), and I is the area moment of inertia (mm^4). R was calculated by fitting a circle to the TEMA points at time 0 using a publicly available MATLAB function based on the Pratt method of least squares fitting of algebraic surfaces [31]. Furthermore, e is defined as:

$$e \approx \frac{I}{RCt.Ar}, \text{ for } \frac{R}{d} > 8 \tag{4}$$

where d is the depth of the cross section. Based on the experimental setup, M can be defined as:

$$M = F_x H - F_y D + M_z, \tag{5}$$

where H and D are the time-dependent moment arms (mm) for the F_x and F_y , respectively, and M_z is the moment about the z-axis (Nmm). Therefore, the bending stress can be defined as:

$$\sigma_b = \frac{M(R^2 - \frac{I}{Ct.Ar} - Rc)}{Ic}, \quad (6)$$

Consequently, the total stress, σ_{tot} (MPa), for any given cross-section can be defined as:

$$\sigma_{tot} = \sigma_n + \frac{M(R^2 - \frac{I}{Ct.Ar} - Rc)}{Ic}, \quad (7)$$

The constant geometric parameters ($Ct.Ar$, I , c) in the above equation were imported directly into the code. The curved beam calculations make several assumptions including: the planar cross-sections of the beam remain planar during bending, there is a longitudinal plane of symmetry along the length of the beam, the beam deflections are small, the bending in the plane of curvature is about a principal axis, and the stresses and strains remain within the elastic region. It was also assumed that the strain measured by the strain gage was equal to the strain at the location of fracture where the geometric parameters were calculated. The stress for the given cross-section was then calculated and plotted against the strain measured by the gages (Figure 3). The resulting curves were then fit to a continuous piecewise model in which the transition strain, k , of the model was chosen to optimize the fit of the model to the data:

$$\sigma(\varepsilon) = \begin{cases} A\varepsilon + D & 0 \leq \varepsilon \leq k \\ B\sin(C\varepsilon + E) & \varepsilon > k \end{cases}, \quad (8)$$

where $\sigma(\varepsilon)$ is stress (MPa) as a function of strain (unitless), A is the elastic modulus (MPa), B is the amplitude of the plastic region (MPa), and C is the frequency of the plastic region (unitless). D and E do not have physical meaning but are used to provide stress magnitude shifting in the elastic region and phase shifting of the plastic region, respectively, to maximize fit. It is important to note here that while these parameters are not directly assigned to a specific material property, they are useful for characterizing properties such as toughness, yield strength, and ultimate strength. Lastly, k is the strain at which the model transitions from elastic to plastic behavior. The transition strain was determined by calculating fit for each point between 30% and 80% of the data as the k value, and the k that yielded the highest R^2 for the entire model was used as the transition strain. Optimization was determined by the least squared norm of the residual. The amount of plastic strain was then determined by the difference between the maximum strain and the starting plastic strain at k . Constraints and initial guesses were applied to the optimization process to ensure that the model was utilizing parameters that not only optimized fit but also made physical sense. A , B , and C were constrained to be positive, while E was bound from negative to positive infinity. The initial guess for A was the slope of the linear portion of the curve and was calculated for each k value for each stress-strain curve. The initial guess for B was 300 MPa and the initial guesses for C and E were both 0 strain which were chosen based on the average values during initial testing of the model. In order for the piece-wise model to be continuous, D was solved for using the other four parameters and thus there were no initial bounds for D .

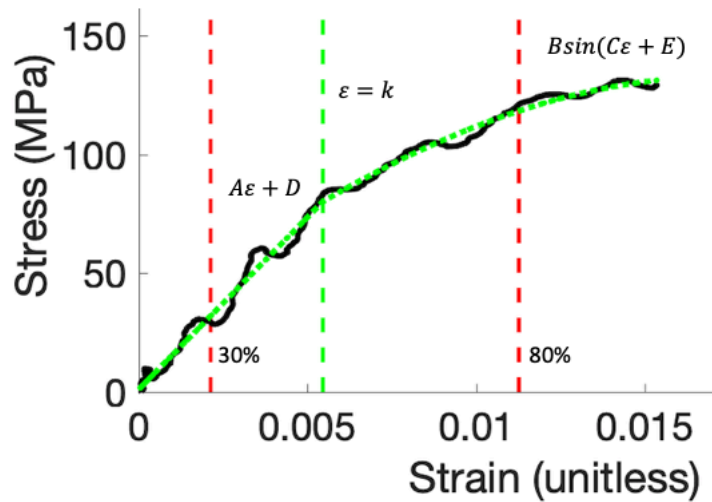


Fig. 3. Stress-strain curve with raw data (black) and fit model (green dotted). The transition point (green dashed) between the elastic and plastic regions is within 30% to 80% (red dashed) of maximum strain.

III. RESULTS

Figure 4 shows an example stress profile which exhibits the stress values calculated at a specific point along the curve length of the rib throughout the duration of the test. The proposed method for creating stress-strain curves yielded a model which resulted in a high degree of fit across the entire sample ($n=30$) with a mean R^2 of 0.995 ± 0.004 ($0.985 - 0.999$) (see Figure 5 for example fit). Due to the high degree of fit, elastic modulus could be directly extracted from the slope of the linear region (A). The mean elastic modulus was found to be 17.42 ± 11.08 GPa ($2.04 - 55.35$). Furthermore, the plastic region was characterized by plastic amplitude (B) and plastic frequency (C). The mean plastic amplitude was 277.33 ± 332.10 MPa ($66.21 - 1818.80$), and the mean plastic frequency was 72.06 ± 57.30 strain⁻¹ ($1.93 - 249.15$). See Appendix for model fit results for each rib test.

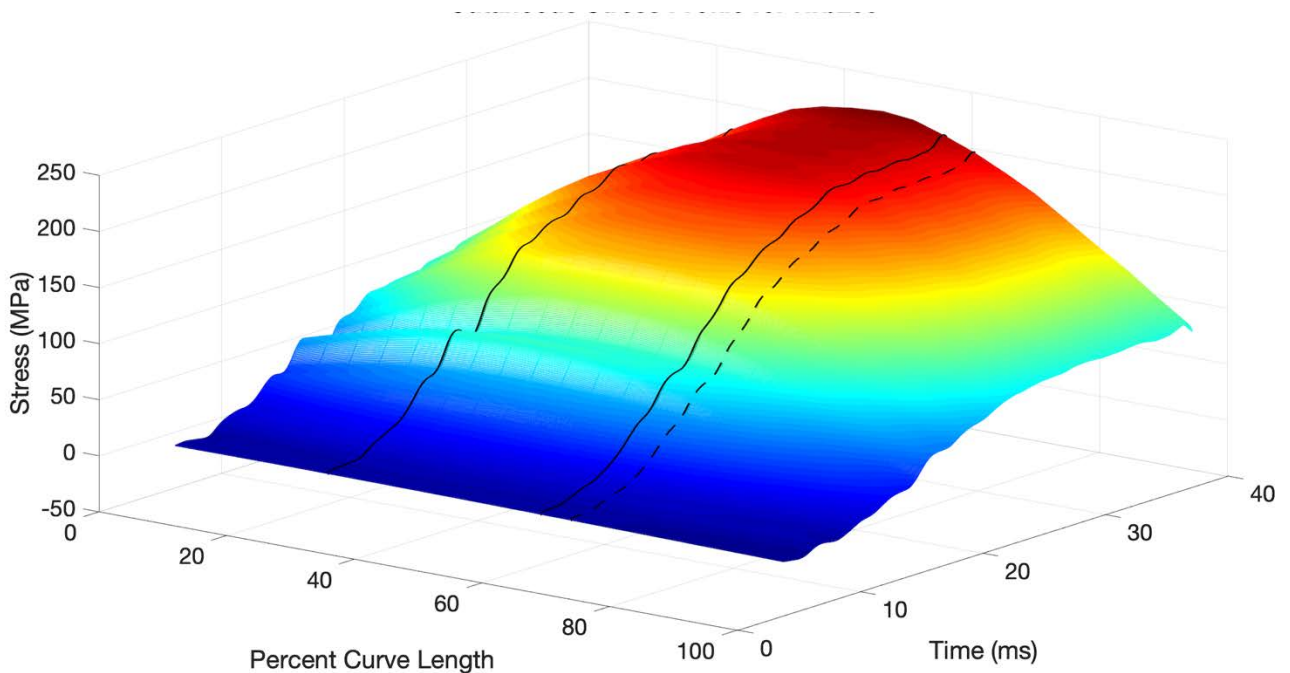


Fig. 4. An example of a rib stress profile along the curve length of the rib throughout the duration of a rib test. Darker shade denotes higher stress. The solid lines represent the locations of the strain gages and the dashed line is the location of the fracture cross-section for the stress calculation.

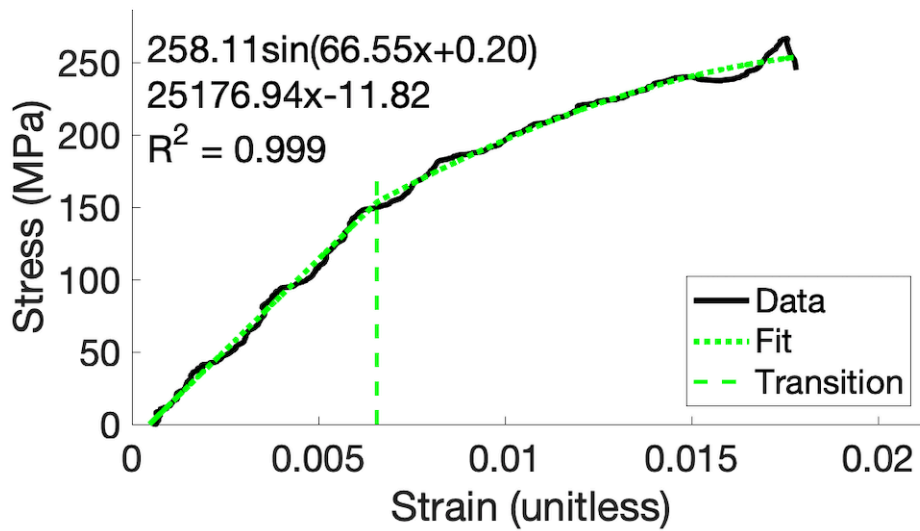


Fig. 5. Example stress-strain curve from a rib test. Curve and model calculated for the cutaneous gage at location 2. Piecewise model parameters are included.

IV. DISCUSSION

The method proposed in this study is applicable for determining force and bending moments at a point on the rib for the entire duration of the test which in turn can be used to calculate stress at that point, given known cortical area (*Ct.Ar*), area moment of inertia (*I*), radius of the cross section (*c*), and the radius of curvature of the rib (*R*). This can be extremely useful for characterizing the stresses present on the rib and explaining rib behavior as seen in Figure 4 (example stress profile). Additionally, Young’s modulus was calculated using the stress-strain curves determined by geometrical calculations about the centroidal axis of the cross-section parallel to the 2D bending axis shown in Figure 2.

For further validation of the model, the structural test outputs of the present model were compared with material testing results from the literature. In the current study, one cutaneous (tensile) gage was used to create a stress-strain curve and model. This allows for direct comparison to the tension coupon material data from the same subjects included here that were recently published by Katzenberger *et al.* [8] and earlier in Albert *et al.* [5] at a consistent strain rate of 0.5 strain/sec.

TABLE I COMPARISON OF MATERIAL PROPERTIES				
	Current Study		Katzenberger <i>et al.</i> [8]	
	Mean	Standard Deviation	Mean	Standard Deviation
Failure Stress (MPa)	161.67	88.24	113.90	35.40
Failure Strain (strain)	0.0123	0.0042	0.0235	0.0082
Elastic Modulus (GPa)	17.42	11.08	13.84	3.71

Table I shows a higher failure stress and lower failure strain in the current study’s structural test than in the material tests from Katzenberger *et al.* [8]. The strain measured by the strain gage in the structural test was not always at the location of fracture. The assumption in this study that the strain was the same at the fracture location is likely why the recorded rib strain during the structural tests was lower compared to the coupon tests. In addition, the coupon tests loaded the ribs in pure uniaxial tension, while the whole ribs experienced combined loading during the structural tests due to the complex geometry of the rib. This combined loading may have caused the ribs to fracture at a lower measured strain than was experienced in the coupon tests. Additionally, the beam equations used in the current study assumed only linear elastic behavior, but the structural test included plastic behavior. This assumption led to increased ultimate stress observed in the structural tests compared to the coupon test[5][8]. Also, trabecular bone was present in the structural tests, whereas the material

tests consisted strictly of cortical bone. This addition of trabecular bone likely led to an increased calculated failure stress as there is a larger cross-sectional area than just the cortical area used in the stress equations. While the curved beam equations do take into account the global geometry of the rib using the radius of curvature, the assumption that the radius of curvature is constant along the length of the rib also likely resulted in an increased total stress calculation and thus an increased elastic modulus as compared to the coupon tests.

Additionally, other previous work on ribs tested at the same strain rate (0.5 strains/sec) showed a significant difference ($p < 0.01$) between means of elastic moduli calculated from coupon (material) and three-point bending (structural) tests performed on matched pairs with means of 14.38 GPa and 20.02 GPa, respectively [8]. Comparing this to the means of 13.84 GPa and 17.19 GPa ($p < 0.001$) (Table I) calculated for elastic modulus from material and structural tests in the current study suggests that the methods used in the present study to create and model stress-strain curves from dynamic whole rib structural tests overestimate the elastic modulus in the same way the three-point bending calculations did in Kemper *et al.* [9]. The model exhibited a high degree of fit across a wide variety of curve shapes with both high and low frequency content. Visually, high frequency content can be readily observed in the strain data, and low frequency content can be observed in the force and moment data. This robustness of the model for a wide range of frequency content enabled the calculated parameters of the model to be directly assigned to a material property, e.g. A is elastic modulus. The high degree of fit also enables the characterization of the entire plastic region of the curve via plastic amplitude (B) and plastic frequency (C). This high degree of fit for a large frequency range suggests that the model could be expanded to fit a larger data set.

The Ramberg-Osgood (9) equation is often used to approximate stress-strain curves for engineering materials when material properties are known [32]:

$$\varepsilon = \frac{\sigma}{E} + K\sigma^n, \quad (9)$$

where σ is the total stress, K is the material parameter, and n is the shape factor material parameter. While the Ramberg-Osgood equation is an established method for estimating stress-strain curves from material properties, it does not allow for a complete characterization of stress-strain curves that exhibit decreasing stress past the ultimate stress in the plastic region. Stress decreases in the plastic region because the stress equations used in this method create engineering stress-strain curves rather than true stress-strain curves. Therefore, since some of the curves created by this model did not have ultimate stress and fracture stress at the same point, the model presented in this study is a preferable method to accommodate these curves.

One common behavior across the stress-strain curves in this study is the presence of strain hardening. The B parameter of the model describes the amplitude of the plastic region as do the values of K or n in the Ramberg-Osgood equation. Therefore, a relationship should exist between these three parameters, meaning that B is a descriptor of strength in the plastic region. Both the K and n terms represent work hardening characteristics. As B results in nonlinear behavior of the plastic region, strain hardening occurs in the ribs. Thus, B can be a descriptor of how local micro-displacements in the bone result in strain hardening. Additionally, the plastic region is characterized by C , the plastic frequency. Changes in the n parameter indicate changes in plastic flow behavior while changes in the K parameter indicate that the magnitude of strength is affected by strain rate. The C parameter also describes the plastic behavior of the rib and there may be a link between this parameter and the plastic flow behavior or strength of the rib. Given that the plastic region is quantified by the two parameters together, neither B nor C are independently able to describe the nonlinear portion of the curve. However, in the context of the proposed model, together B and C are needed to describe these parameters using the nonlinear portion of the model as the model fits the data with a high degree of accuracy. A future research area could be quantifying the relationships between the B , C , K , and n parameters.

Several limitations exist with the current model. Boundary conditions of the experiment were designed to ensure repeatable loading; however, they do not represent the exact position of the rib within the human thorax as only 2D movement was captured. The current study only considered the stress calculated at the cross-section of the fracture that was closest to the cutaneous (tension) gage at location 2. Future work will incorporate the other strain gages and fractures and include pleural (compression) calculations in order to quantify where the maximum stress occurs. The histological cross-sections were taken directly adjacent to the fracture site and were not at the exact location of a strain gage, so the strain values measured at the gage were simply assumed to be

the same as those at the histological cross-section. This difference in strain from the gage to the fracture location likely causes the failure strain to be underestimated, and thus the elastic modulus to be overestimated, in the current study. Future work will address this by defining a transfer function to calculate strain at other points on the rib from the strain gages. In addition, the assumption that the radius of curvature is constant along the length of the rib, and the simple circle fitting method of calculating the radius of curvature, likely causes this measurement to be overestimated. Consequently, the total stress calculations are being overestimated which is likely causing the elastic modulus to be overestimated as well. Future work will focus on utilizing the novel rib shape model presented by Holcombe et al. [33] to more accurately calculate the radius of curvature. Also the beam equations used in this model assumed only linear-elastic deformation which is not the case for the current structural rib tests that were conducted until failure. This assumption did not have a negative impact on the elastic modulus calculation, however future work will focus on investigation into the impact it may have had on the plastic region.

Additionally, the cortical area and radius for the cortex were assumed to be constant along the length of the rib in this model, which is not realistic. Therefore, stress can only be calculated at a point where the cortical area and section radius are known. Future work will explore utilizing this method for creating discrete stress profiles with accurate cross-sectional geometry along the entire length of the rib utilizing novel imaging techniques presented by Holcombe et al. [34] instead of assuming a constant cross-sectional geometry. This will allow for further examination of where the maximum stress along the length of the rib occurs. Furthermore, the uni-axial strain gages only captured strain along the longitudinal axis of the rib, so any off-axis strains were not captured. Additionally, there were likely damping effects along the length of the rib which would introduce some error in the force transform. As discussed previously, the present model calculates the stress on cortical bone in the rib ($Ct. Ar$ and I for cortical bone), yet the force measured was distributed across the entire rib including cortical and trabecular bone and bone marrow. The parameters $Ct. Ar$ and I were calculated assuming that cortical bone is a solid, homogenous bone i.e., no pores are present. Future work should examine the contribution of trabecular bone and pores to the overall stress-strain response of the rib by including these parameters in the calculation of $Ct. Ar$ and I [35] and further increasing the accuracy of the stress calculation. Furthermore, planar motion was assumed because the spatial orientation of the rib could only be tracked in two dimensions. Therefore, only forces corresponding with these dimensions were considered. All out-of-plane forces and moments were small compared to F_x so it is reasonable to make this planar assumption. However, devising a method for incorporating all directions of motion would lend itself to increasing the accuracy of the stress calculations.

The present preliminary study created a method for calculating stress-strain curves from structural, dynamic bending tests, and proposed a continuous piecewise model to quantify the resulting stress-strain curves. Material properties of ribs, including elastic modulus, are used in finite element models, but prior to the current study these properties could only be obtained from material tests. Creating a link between material properties from structural tests to material properties from coupon tests is useful because structural tests have been performed on a larger data set. The current model can be applied to the large, existing data set of structural tests that includes subjects from a wide range of demographics. Applying the model to this dataset would help describe the variation in material properties between individuals, and the resulting material parameters could be linked to which individuals are more or less vulnerable to rib fractures. Additionally, the material properties obtained from this model applied to the large existing dataset could aid in creating better scaling techniques for vulnerable populations. Future work should focus on applying structural test material properties to finite element model simulations of rib structural tests to compare the response of the model with material properties from structural tests to the response with material properties from coupon tests.

V. CONCLUSIONS

The current study presents a novel preliminary method for creating stress-strain curves for human rib cortical bone from structural dynamic bending tests. In addition to the method of calculating stress-strain curves, a continuous piecewise model was proposed for quantifying the curves, consisting of a linear elastic region and a sinusoidal plastic region. The model fit the raw stress-strain curve to a high degree, so material properties were directly extracted from the model. The values of elastic modulus found in the present study were consistent with elastic modulus values calculated from structural tests in previous studies. As with other studies, the elastic modulus values were overestimated due to some of the assumptions made with beam calculations being violated.

Future work is needed to address these assumptions in order to more accurately calculate elastic modulus from structural tests. Once the model has been shown to be more accurate, it can be applied to a large, existing data set for human rib properties which contains a wide variety of demographics. Deriving material properties from structural tests may improve finite element models by increasing the biofidelity of these tools to allow for the design of safer motor vehicles.

VI. ACKNOWLEDGEMENT

The authors would like to thank the anatomical donors and families of the Body Donation Program at The Ohio State University and Lifeline of Ohio for their generous gifts. The National Highway Traffic Safety Administration sponsored this project. Additionally, Autoliv Research sponsored some of the experimental tests which generated data contained within this work. The material data from Katzenberger et al. [8] for direct comparison to the samples used in this study were provided by Andrew Kemper, Devon Albert, and Michael Katzenberger, and we are grateful for the shared data and ongoing collaboration. The views presented here are those of the authors and do not represent those of the any sponsors or funding agencies. We are grateful to the students and staff of the Injury Biomechanics Research Center, especially Reagan Di Iorio, Brianna Marselle, Victoria Dominguez, Zach Eshelman, Laura Jurewicz, Angela Harden, and Arri Willis.

VII. REFERENCES

- [1] Liu, C., Utter, D., Chen, C.L. (2007) Characteristics of Crash Injuries Among Young, Middle-Aged, and Older Drivers. National Highway Traffic Safety Administration (NHTSA), Washington DC, USA. DOT HS 810 857, 2007.
- [2] The Abbreviated Injury Scale. 1990 Revision, Update 98. Association for the Advancement of Automotive Medicine; Des Plaines, Illinois: 1998.
- [3] Kent, R., Woods, W., Bostrom, O. (2008) Fatality risk and the presence of rib fractures. *Proceedings of AAAM Annual Scientific Conference*, 2008. Miami, FL.
- [4] Kim, M. and Moore, J.E. (2020) Chest Trauma: Current Recommendations for Rib Fractures, Pneumothorax, and Other Injuries. *Curr Anesthesiol Rep*, **10**:pp.61-68.
- [5] Albert, D.L., Kang, Y.-S., Agnew, A.M., Kemper, A.R. (2017) A comparison of rib structural and material properties from matched whole rib bending and tension coupon tests. *Proceeding of IRCOBI Conference*, 2017, Antwerp, Belgium.
- [6] Albert, D.L., Kang, Y.-S., Agnew, A.M., Kemper, A.R. (2018) The effect of injurious whole rib loading on rib cortical bone material properties. *Proceeding of IRCOBI Conference*, 2018, Athens, Greece.
- [7] Iraeus, J., Lundin, L., Storm, S., Agnew, A., Kang, Y.-S., Kemper, A., Albert, D., Holcombe, S., Pipkorn, B. (2019) Detailed subject-specific FE rib modeling for fracture prediction. *Traffic Injury Prevention*, **20**:sup2,S88-S95.
- [8] Katzenberger, M. J., Albert, D. L., Agnew, A. M., & Kemper, A. R. (2020). Effects of sex, age, and two loading rates on the tensile material properties of human rib cortical bone. *Journal of the Mechanical Behavior of Biomedical Materials*, *102*, 103410. doi: 10.1016/j.jmbbm.2019.103410
- [9] Kemper, A.R., McNally, C., et al. (2007) The biomechanics of human ribs: Material and structural properties from dynamic tension and bending tests. *Stapp Car Crash Journal*, **51**:pp.235-273.
- [10] Kemper, A.R., McNally, C., et al. (2005) Material properties of human rib cortical bone from dynamic tension coupon testing. *Stapp Car Crash Journal*, **49**(11): pp. 199-230
- [11] Stitzel, J.D., Cormier, J.M., Barretta, J.T., Kennedy, E.A. (2003) Defining regional variation in the material properties of human rib cortical bone and its effect on fracture prediction. *Stapp Car Crash Journal*, **47**: pp. 243-265
- [12] Subit, D., de Dios, EdP, Valazquez-Ameijide, J., Arregui-Dalmases, C., Crandall, J. (2011) Tensile material properties of human rib cortical bone under quasi-static and dynamic failure loading and influence of the bone microstructure on failure characteristics. 2011. <https://arxiv.org/abs/1108.0390>.
- [13] Agnew, A.M., Murach, M.M., et al. (2018) Sources of variability in structural bending response of pediatric and adult human ribs in dynamic frontal impacts. *Stapp Car Crash Journal*, **62**:pp.119-192.
- [14] Agnew, A.M., Schafman, M., Moorhouse, K., White, S.E., Kang, Y-S. (2015) The effect of age on the structural properties of human ribs. *Journal of the mechanical behavior of biomedical materials*, **41**: pp. 302-314
- [15] Charpail, E., Trosseille, X., Petit, P., and Laporte, S. (2005) Characterization of PMHS ribs: a new test methodology. *Stapp Car Crash Journal*, **49**: pp. 183-198.

- [16] Cormier, J.M., Stitzel, J.D., Duma, S.M., and Matsuoka, F. (2005) Regional variation in the structural response and geometrical properties of human ribs. *Annual Proceedings of the Association for the Advancement of Automotive Medicine*, 2005.
- [17] Granik, G. and Stein, I. (1973) Human ribs: static testing as a promising medical application. *Journal of Biomechanics*, **6**(3): pp. 237-240
- [18] Kindig, M., Lau, A.G., and Kent, R.W. (2011) Biomechanical response of ribs under quasistatic frontal loading. *Traffic injury prevention*, **12**(4): pp. 377-387
- [19] Sacreste, J., Brun-Cassan, F., et al. (1982) Proposal for a thorax tolerance level in side impacts based on 62 tests performed with cadavers having known bone condition. *Proceedings of 26th Stapp Car Crash Conference*, 1982.
- [20] Stein, I. and Granik, G. (1976) Rib structure and bending strength: an autopsy study. *Calcified Tissue International*, **20**(1): pp. 61-73
- [21] Yoganandan, N. and Pintar, F. (1998) Biomechanics of human thoracic ribs. *Transactions-American Society of Mechanical Engineers Journal of Biomechanical Engineering*, **120**: pp. 100-105
- [22] Kalra, A., Saif, T., et al. (2015) Characterization of Human Rib Biomechanical Responses due to Three-Point Bending. *Stapp Car Crash Journal*, 2015. **59**: pp. 113-130
- [23] Tomasch, E., Kirschbichler, S., et al. (2010) Methodology to predict thresholds for loading corridors of human ribs. *Proceedings of International Research Council on the Biomechanics of Injury Conference*, 2010. Hanover, Germany.
- [24] Schafman, M.A., Kang, Y.-S., et al. (2016) Age and sex alone are insufficient to predict human rib structural response to dynamic AP loading. *Journal of Biomechanics*, 2016. **49**(14): pp. 3516-3522
- [25] Duma, S., Stitzel, J., et al. (2005) Non-censored rib fracture data from dynamic belt loading tests on the human cadaver thorax. *Proc. 19th International Technical Conference on the Enhanced Safety of Vehicles*. Washington, DC: NHTSA, 2005.
- [26] Murach, M.M., Kang, Y.-S., et al. (2017) Rib Geometry Explains Variation in Dynamic Structural Response: Potential Implications for Frontal Impact Fracture Risk. *Annals of Biomedical Engineering*, **45**(9):pp.2159-2173.
- [27] Dominguez, V., & Agnew, A.M. (2019) The use of ROI overlays in a semi-automated method for measuring cortical area in ImageJ for histological analysis. *American Journal of Physical Anthropology*, **168**: pp.378-382.
- [28] Romani, W.A., Gieck, J.H., Perrin, D.H., Saliba, E.N., and Kahler, D.M. (2002) Mechanisms and Management of Stress Fractures in Physically Active Persons. *Journal of Athletic Training*, **37**(3):pp.306-314
- [29] SAE. (2007) Instrumentation for impact test-part 1-electronic instrumentation, J211/1. Warrendale, PA.
- [30] Young, W.C., Budynas, R.G. *Roark's Formulas for Stress and Strain*. New York, NY: McGraw-Hill.
- [31] Pratt, V. (1987) Direct least-squares fitting of algebraic surfaces. *Computer Graphics (SIGGRAPH '87 Proceedings)*, **21**(4):pp.145-152.
- [32] McIellan, D. L. (1967). Constitutive equations for mechanical properties of structural materials. *AIAA Journal*, **5**(3): pp.446-450.
- [33] Holcombe, S.A., Wang, S.C., Grotberg J.B. (2016) Modeling female and male rib geometry with logarithmic spirals. *Journal of Biomechanics*, **49**:pp.2995-3003.
- [34] Holcombe, S.A., Hwang, E., Derstine, B.A., Wang, S.C. (2018) Measuring rib cortical bone thickness and cross section from CT. *Medical Image Analysis*, **49**:pp. 27-34;
- [35] Dominguez, V., Kang, Y.-S., Murach, M., Crowe, N., Agnew, A.M. (2016) Bone area vs cortical area: Considering intracortical porosity when predicting rib structural properties. *Paper presented at the International Research Council on Biomechanics of Injury*, 2016, Malaga, Spain.

VIII. APPENDIX

All units in the following plots for the A, B, and D parameters are in MPa.

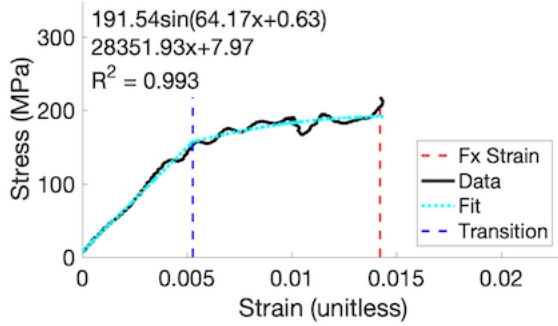


Fig. A1. Hrb167 stress-strain curve.

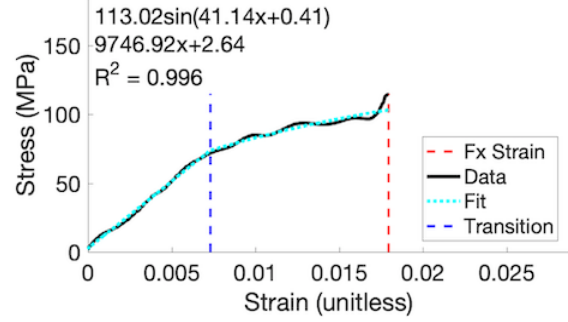


Fig. A2. Hrb175 stress-strain curve.

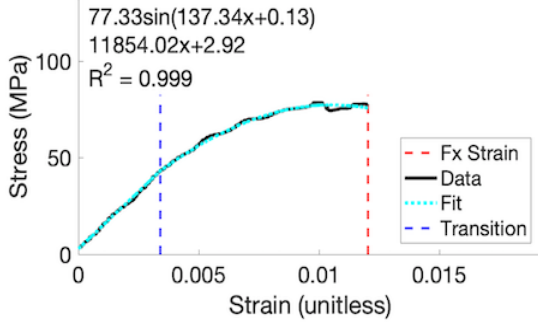


Fig. A3. Hrb180 stress-strain curve.

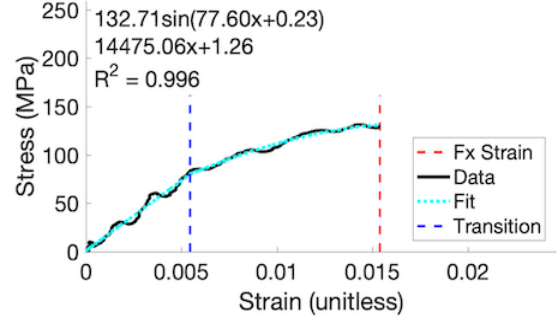


Fig. A4. Hrb219 stress-strain curve.

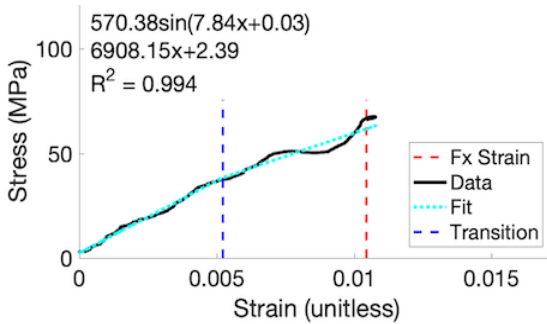


Fig. A5. Hrb220 stress-strain curve.

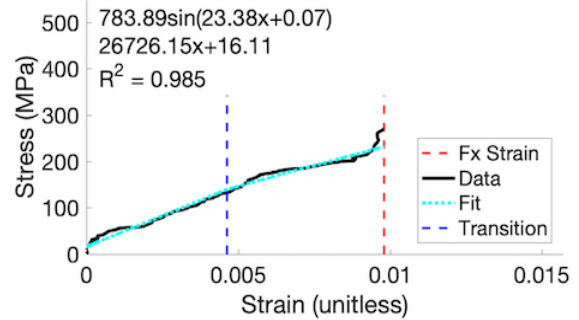


Fig. A6. Hrb221 stress-strain curve.

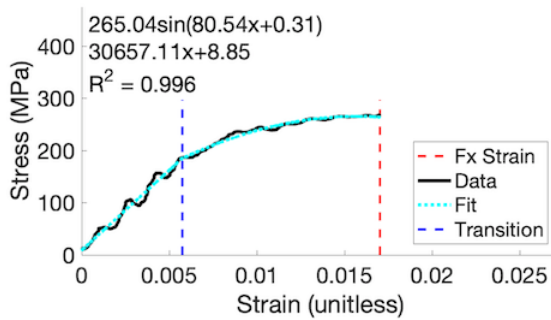


Fig. A7. Hrb222 stress-strain curve.

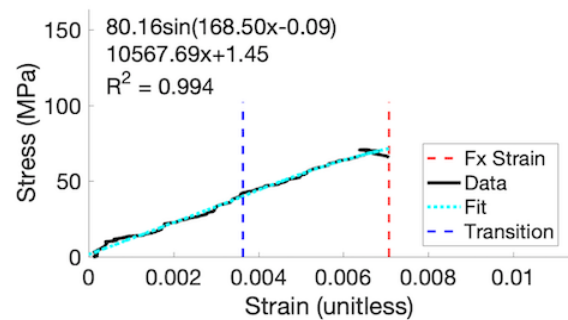


Fig. A8. Hrb223 stress-strain curve.

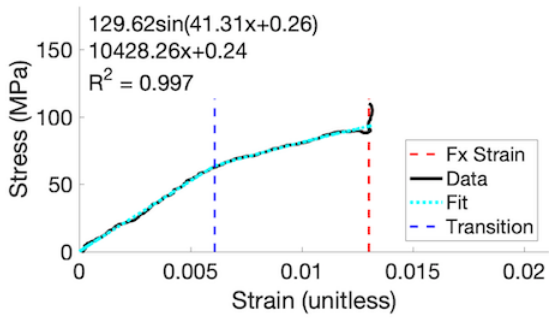


Fig. A9. Hrb224 stress-strain curve.

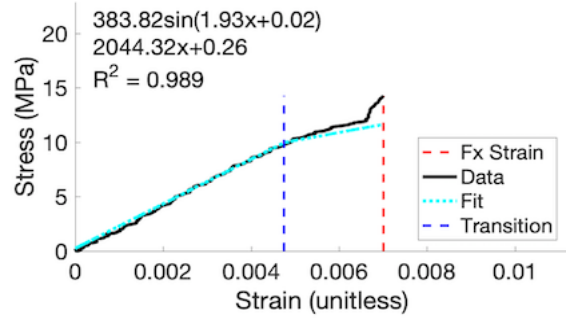


Fig. A10. Hrb225 stress-strain curve.

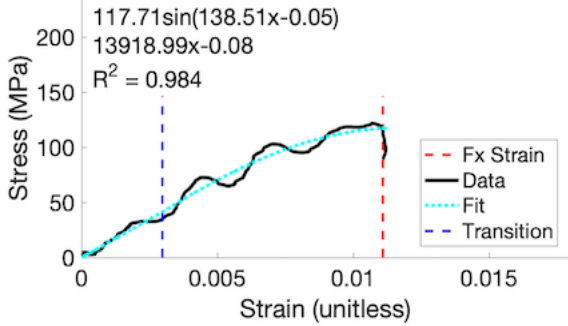


Fig. A11. Hrb226 stress-strain curve.

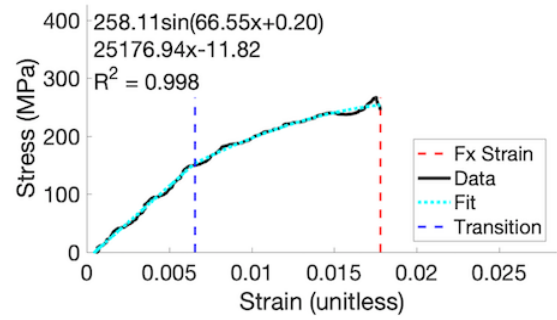


Fig. A12. Hrb227 stress-strain curve.

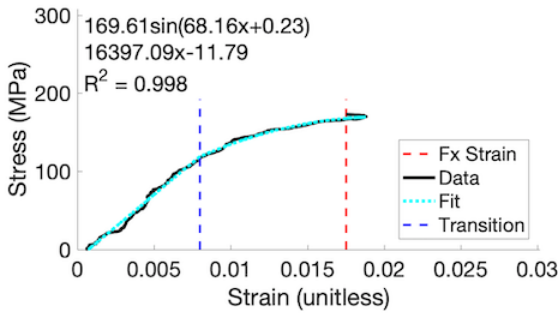


Fig. A13. Hrb228 stress-strain curve.

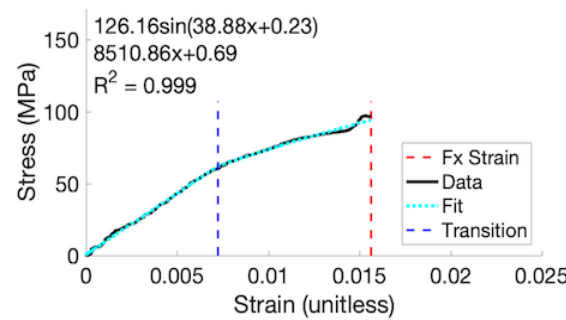


Fig. A14. Hrb229 stress-strain curve.

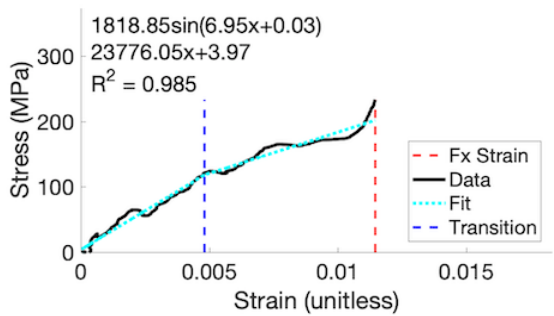


Fig. A15. Hrb231 stress-strain curve.

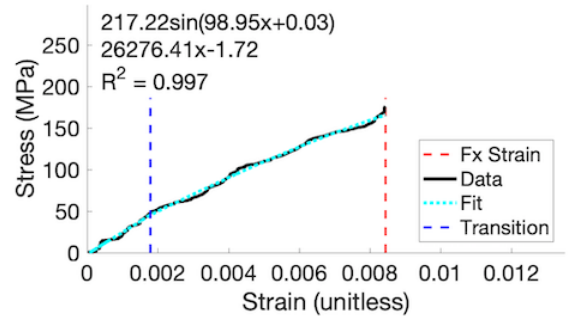


Fig. A16. Hrb233 stress-strain curve.

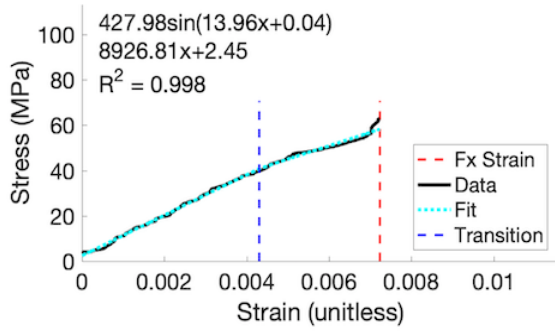


Fig. A17. Hrb234 stress-strain curve.

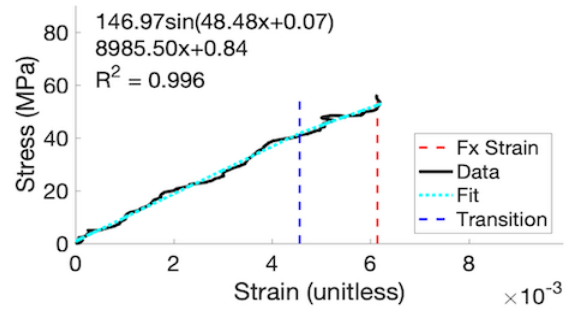


Fig. A18. Hrb235 stress-strain curve.

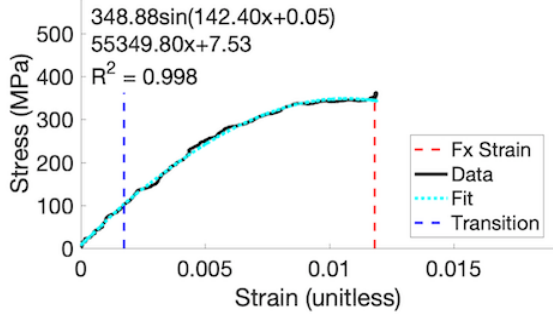


Fig. A19. Hrb238 stress-strain curve.

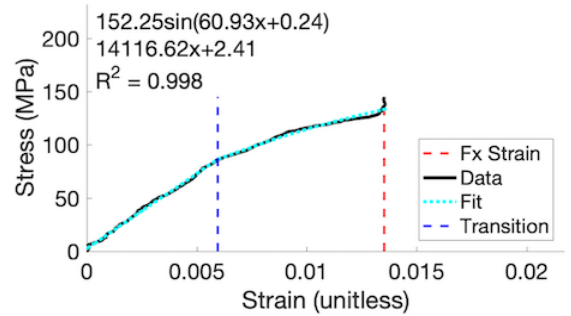


Fig. A20. Hrb239 stress-strain curve.

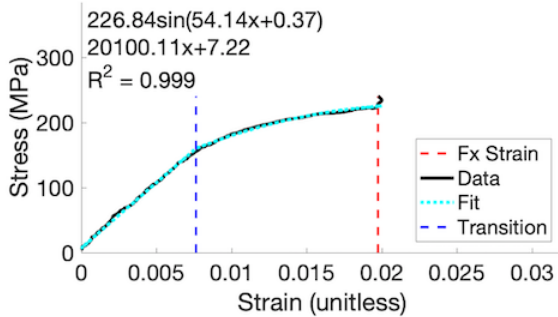


Fig. A21. Hrb240 stress-strain curve.

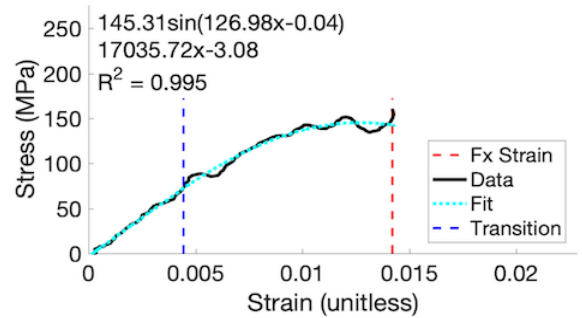


Fig. A22. Hrb242 stress-strain curve.

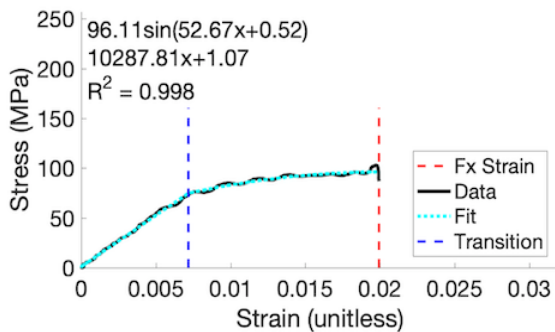


Fig. A23. Hrb244 stress-strain curve.

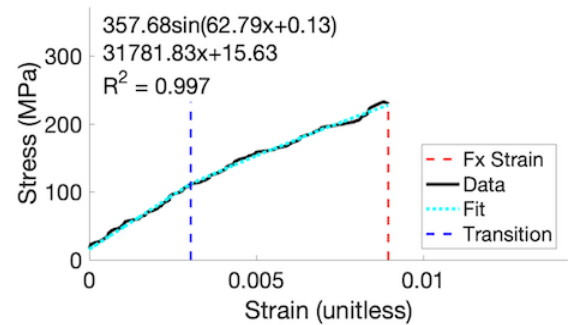


Fig. A24. Hrb245 stress-strain curve.

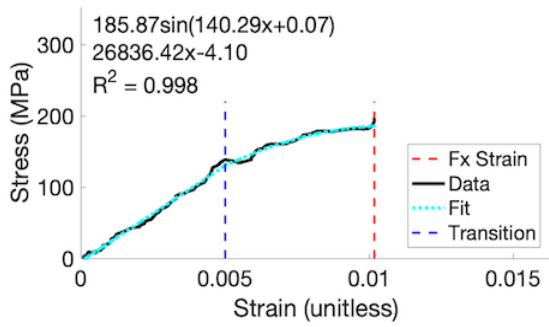


Fig. A25. Hrb246 stress-strain curve.

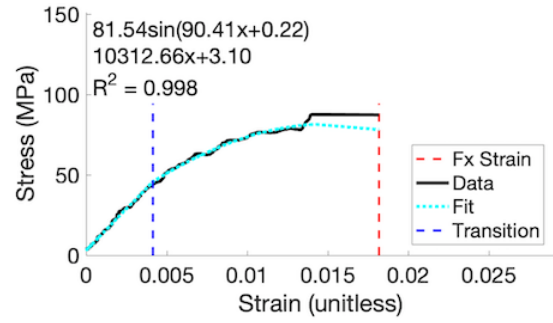


Fig. A26. Hrb247 stress-strain curve.

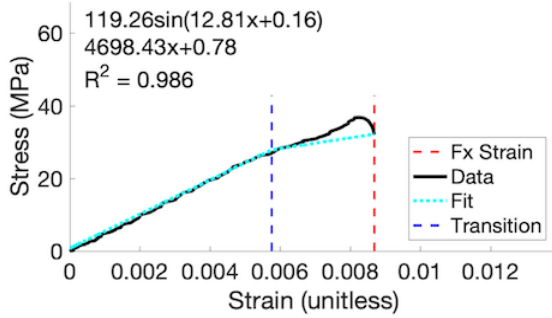


Fig. A27. Hrb248 stress-strain curve.

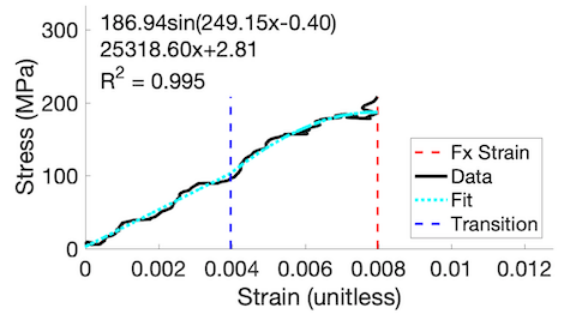


Fig. A28. Hrb249 stress-strain curve.

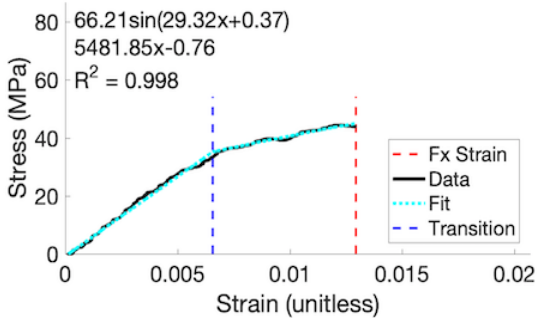


Fig. A29. Hrb250 stress-strain curve.

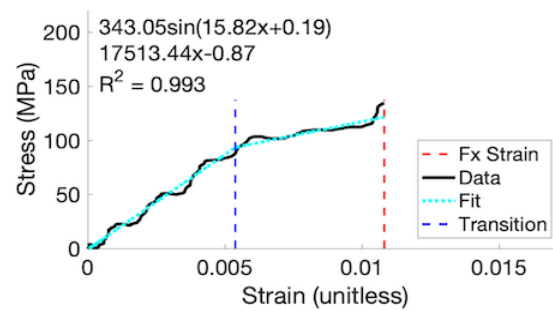


Fig. A30. Hrb251 stress-strain curve.